Three dimensional thermal-, electrical-, and electrochemical-coupled model for cylindrical wound large format lithium-ion batteries

Kyu-Jin Lee [a,b], Kandler Smith [a], Ahmad Pesaran [a], Gi-Heon Kim [a,*]

[a] National Renewable Energy Laboratory, 15013 Denver West Parkway, Golden, CO, USA
[b] Department of Mechanical Engineering, Myongji University, 116 Myongji-ro Cheoin-gu, Yongin-si, Gyeonggi-do, South Korea

HIGHLIGHTS

- The wound potential-pair continuum (WPPC) model is developed.
- It serves a cell-domain model of the Multi-Scale Multi-Domain (MSMD) framework.
- It resolves temperature and current collector phase potential variation in cell composites.
- It is coupled with submodels solving lithium diffusion dynamics and kinetics.
- Electrical/electrochemical/thermal coupled behavior of 20 Ah cylindrical cells was investigated.

ARTICLE INFO

ABSTRACT

A numerical model for cylindrical wound lithium-ion cells, which resolves thermal, electrical and electrochemical coupled physics, is presented in this paper. Using the Multi-Scale Multi-Domain (MSMD) model framework, the wound potential-pair continuum (WPPC) model is developed as a cell domain submodel to solve heat and electron transfer across the length scale of cell dimension. By defining the cell composite as a wound continuum, the WPPC model can evaluate layer-to-layer differences in electrical potential along current collectors, and electric current in the winding direction to investigate the effects of thermal and electrical configurations of a cell design, such as number and location of tabs, on performance and life of a cylindrical cell. In this study, 20-Ah large-format cylindrical cell simulations are conducted using the WPPC model with the number of electrical tabs as a control parameter to investigate how macroscopic design for electrical current transport affects microscopic electrochemical processes and apparent electrical and thermal output.

© 2013 Elsevier B.V. All rights reserved.

1. Introduction

To meet the system demands of high-energy and high-power energy storage in electric vehicle applications, lithium-ion cells with increased size and capacity have the advantage of reducing the number of interconnectors and control circuits when integrated in a battery pack. Although the technology of small lithium-ion batteries (LIBs) for consumer-electronic devices has made significant progress regarding performance, cost, life, and safety in the past 20 years, the scale-up of batteries is still challenging because of unexpected size effects. As cell size increases, spatial non-uniformity of temperature and current collector electrical

potential in a cell excessively grows and significantly influences electrical, thermal, electrochemical, and mechanical response of a LIB system. Thus, without knowledge of the interplays among interdisciplinary multi-physics occurring across varied length scales in LIB systems, it is difficult to design long-lasting, high-performing, large-format LIB cells retaining the quality of small capacity LIB systems. Cylindrical cell formats, widely adopted by the consumer electronics battery market because of their low production cost and well-established manufacturing process, face difficulties in scaling-up capacity. One well known issue is poor thermal characteristics, such as decreased surface-to-volume ratio and increased radial dimension of cells. The adverse impacts of non-optimized electrical pathway design on cell performance and degradation become significant in such a scenario. In a typical large-format cylindrical cell with discrete electrical tabs, electrical pathways carrying current along continuous wound metal foil are longer, causing excessive non-uniformity in kinetics and transport.

* Corresponding author. Tel.: +1 303 275 4437; fax: +1 303 275 4415.
E-mail addresses: gi-heon.kim@nrel.gov, kgheon@gmail.com (G.-H. Kim).

To avoid unexpected loss of cell performance in large-format designs, it is important to know how thermal and electrical design of large-scale cylindrical cells affects cell physics. The build-and-break design process, typically used by the battery manufacturing industry, is costly, extremely time-consuming for large-format cells, and provides only limited information. In contrast, numerical models which resolve the interactions between long-range transport and short-range physics can help to shorten design processes and optimize batteries. Since Newman and his team [1] suggested a numerical model for a LIB resolving lithium diffusion dynamics and charge transfer kinetics in porous electrodes, various mathematical approaches [2,3] have been used to understand physics in LIB systems and predict their electrical response. However, it is challenging to extend these approaches to simulate large capacity system responses. Most numerical models for wound cells suggest various simplification strategies to achieve effective solutions [4–14]. Previous studies on heat conduction in spirally-wound geometry assumed uniform kinetics throughout the cell volume, with volumetric heat generation evaluated from experimental data [4–7] or from a lumped cell model [8–10]. Heat conduction in cylindrical cells has been studied in various simplified geometry models: lumped thermal mass [4], 1-D radial direction [7,8], 2-D spiral geometry [5,6,11], 1-D radial spiral modeling with the domain reduced from a 2-D spiral model through the coordinate-transform technique [12], 2-D concentric rings [9], and 3-D concentric rings [10]. On the other hand, several studies only solved electrical current along wound metal current collectors assuming uniform kinetics over a cell volume without temperature calculation [13,14]. To date, there has not been a numerical study solving a thermal-, electrical-, and electrochemical-coupled system in a 3-dimensional cell domain resolving spirally-wound geometry.

In our previous study by Kim et al. [15], we introduced the Multi-Scale Multi-Domain (MSMD) model framework, able to investigate the interplay among various length scale physics in lithium-ion batteries by decoupling submodel geometries. In the MSMD framework, electric potential variation along current collectors and heat transfer are solved in a computational domain representing the battery cell length-scale, coupled with lithium diffusion dynamics and charge transfer kinetics in smaller length-scale subdomains. In this paper, we introduce development of the wound potential-pair continuum (WPPC) model, a cell domain submodel of the MSMD framework, and apply the model to investigate electrical, thermal and electrochemical behaviors of large-format cylindrical wound cells.

2. Model description

The computational model geometries of the MSMD framework are separated into a particle domain, an electrode domain and a cell domain. Model geometries in each domain are completely decoupled and the solution variables are solved for corresponding length-scale physics while coupled through inter-domain communication between the adjacent hierarchical model domains. The solution variables in each domain and the inter-domain coupling quantities are summarized in Fig. 1. The MSMD model framework solves lithium diffusion inside solid electrode particles and charge transfer kinetics in the particle domain. Charge balance in solid matrices and the liquid phase, as well as species transport across the electrode pair are solved in the electrode domain. In the cell domain, electrical current flow in metal current collector sheets and heat flow over a cell composite volume are calculated in consideration of macroscopic cell geometries and boundary conditions. Thanks to its modularized hierarchical architecture, the MSMD framework allows flexible choice of submodels in each modeling domain. In this study, the submodel chosen for the particle domain model is a one-
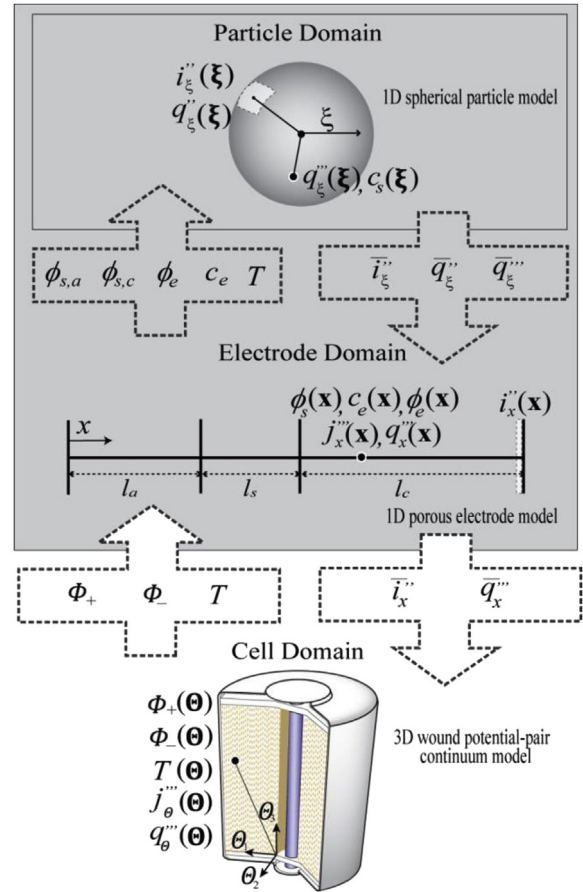

Fig. 1. The MSMD model framework: summary of submodel choice, solution variables in each submodel domain, and coupling variables.

dimensional spherical particle model, and the submodel chosen for the electrode domain is a one-dimensional porous electrode model as presented in Fig. 1. The governing equations of the particle domain and the electrode domain are summarized in Table 1. A model-reduction scheme, the state variable model (SVM), which calculates the governing equations as a quasi-linear system, is adopted to enhance computational speed [16]. Detailed information regarding the submodels and the MSMD framework is found in Kim et al. [15].

2.1. Wound cell geometry

Cylindrical lithium-ion cells typically have a pair of long, wide continuous current collectors wound as shown in Fig. 2. As electrical current generated from charge transfer kinetics across the pair of electrode layers is delivered through external circuitry, electric current convergence causing large potential change occurs near the electrical tabs. Where a cell has extended foils functioning as continuous tabs in Fig. 2(a), electric current mainly flows in the axial direction of the jelly roll, wound with negligible difference of electrical potential in the azimuthal direction. For continuous tab-bed cells, it is reasonable to represent an arbitrary finite volume of jelly roll with a single pair of electric potentials to define a single potential-pair continuum (SPPC). On the other hand, in the cell represented in Fig. 2(b), which has discrete and localized electrical terminals, electric current flows in the azimuthal direction, resulting in significant change of electrical potential in the azimuthal direction. This means that electrical potentials in an
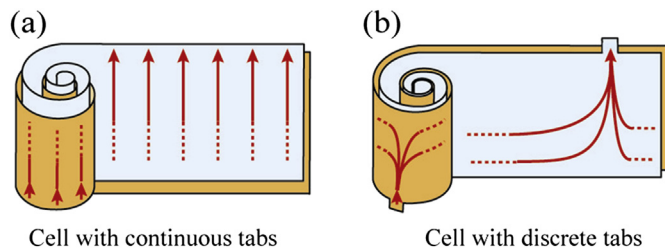
Table 1
Summary of solution variables and governing equations of submodel choices.

Domain	Solution variable	Governing equation	
Particle	Submodel choice: 1D spherical particle model		
	$i''_{\xi}(\xi = R_s, x, r_i, \theta_i, z_i)$	$i''_{\xi} = k_i(c_e)^{\alpha_a}(c_{s,\max} - c_{s,e})^{\alpha_a}(c_{s,e})^{\alpha_c}\left\{\exp\left[\frac{\alpha_a F}{RT}\eta\right] - \exp\left[-\frac{\alpha_c F}{RT}\eta\right]\right\}$	
	$c_s(\xi, x, r_i, \theta_i, z_i)$	$\frac{\partial c_s}{\partial t} = \frac{D_s}{\xi^2}\frac{\partial}{\partial\xi}\left(\xi^2\frac{\partial c_s}{\partial\xi}\right)$	B.C.) $\frac{\partial c_s}{\partial\xi}\big|_{\xi=0} = 0, \ \frac{\partial c_s}{\partial\xi}\big|_{\xi=R_s} = \frac{-i''_{\xi}}{D_s F}$
Electrode	Submodel choice: 1D porous electrode model		
	$c_e(x, r_i, \theta_i, z_i)$	$\frac{\partial(\varepsilon_e c_e)}{\partial t} = \frac{\partial}{\partial x}\left(D_e^{\text{eff}}\frac{\partial}{\partial x}c_e\right) + \frac{1-t_+^o}{F}j''_x - \frac{i''_e}{F}\frac{\partial t_+^o}{\partial x}$	B.C.) $\frac{\partial c_e}{\partial x}\big|_{x=0} = 0, \ \frac{\partial c_e}{\partial x}\big|_{x=l_a+l_s+l_c} = 0$
	$\phi_e(x, r_i, \theta_i, z_i)$	$\frac{\partial}{\partial x}\left(\kappa^{\text{eff}}\frac{\partial}{\partial x}\phi_e\right) + \frac{\partial}{\partial x}\left(\kappa_D^{\text{eff}}\frac{\partial}{\partial x}\ln c_e\right) + j''_x = 0$	B.C.) $\frac{\partial\phi_e}{\partial x}\big|_{x=0} = 0, \ \frac{\partial\phi_e}{\partial x}\big|_{x=l_a+l_s+l_c} = 0$
	$\phi_{s,a}(x, r_i, \theta_i, z_i)$	$\frac{\partial}{\partial x}\left(\sigma^{\text{eff}}\frac{\partial}{\partial x}\phi_s\right) - j''_x = 0$	B.C.) $\phi_{s,a}\big|_{x=0} = \Phi_-, \ \frac{\partial\phi_{s,a}}{\partial x}\big|_{x=l_a} = 0$
	$\phi_{s,c}(x, r_i, \theta_i, z_i)$	$\frac{\partial}{\partial x}\left(\sigma^{\text{eff}}\frac{\partial}{\partial x}\phi_s\right) - j''_x = 0$	B.C.) $\frac{\partial\phi_{s,c}}{\partial x}\big|_{x=l_a+l_s} = 0, \ \phi_{s,c}\big|_{x=l_a+l_s+l_c} = \Phi_+$
Cell	Submodel choice: 3D single potential-pair continuum (SPPC) model		
	$\Phi_-(r_i, \theta_i, z_i)$	$\left(\frac{\varepsilon_-\sigma_-}{r_-^2}\frac{\partial^2\Phi}{\partial\theta^2} + \varepsilon_-\sigma_-\frac{\partial^2\Phi}{\partial z^2} + j''_-\right)_i = 0$	
	B.C.) $\left(\frac{\varepsilon_-\sigma_-}{r_-^2}\frac{\partial^2\Phi}{\partial\theta^2} + \varepsilon_-\sigma_-\frac{\partial^2\Phi}{\partial z^2}\right)_1\big|_{\theta_1=0,\pi} = \left(\frac{\varepsilon_-\sigma_-}{r_-^2}\frac{\partial^2\Phi}{\partial\theta^2} + \varepsilon_-\sigma_-\frac{\partial^2\Phi}{\partial z^2}\right)_2\big|_{\theta_2=\pi,0}, \ j''_- = -(\overline{i''_x}a_s)_{\text{iep}} - (\overline{i''_x}a_s)_{\text{oep}-}$		
	$\Phi_+(r_i, \theta_i, z_i)$	$\left(\frac{\varepsilon_+\sigma_+}{r_+^2}\frac{\partial^2\Phi}{\partial\theta^2} + \varepsilon_+\sigma_+\frac{\partial^2\Phi}{\partial z^2} + j''_+\right)_i = 0$	
	B.C.) $\left(\frac{\varepsilon_+\sigma_+}{r_+^2}\frac{\partial^2\Phi}{\partial\theta^2} + \varepsilon_+\sigma_+\frac{\partial^2\Phi}{\partial z^2}\right)_1\big|_{\theta_1=0,\pi} = \left(\frac{\varepsilon_+\sigma_+}{r_+^2}\frac{\partial^2\Phi}{\partial\theta^2} + \varepsilon_+\sigma_+\frac{\partial^2\Phi}{\partial z^2}\right)_2\big|_{\theta_2=\pi,0}, \ j''_+ = (\overline{i''_x}a_s)_{\text{iep}} + (\overline{i''_x}a_s)_{\text{oep}+}$		
	$T(r_i, \theta_i, z_i)$	$\frac{\partial(\rho C_p T)}{\partial t} = \left(\frac{1}{r}\frac{\partial}{\partial r}\left(k_{\text{tr}} r\frac{\partial T}{\partial r}\right) + \frac{k_{\text{in}}}{r^2}\frac{\partial^2 T}{\partial\theta^2} + k_{\text{in}}\frac{\partial^2 T}{\partial z^2}\right)_i + q'''_\Theta$	

*i*: index of cell domain coordinates, 1 or 2.

arbitrary finite volume of a cylindrical cell composite cannot be represented with a single pair of electrical potentials, and the wound structure of an electrode composite should be resolved in the model geometry. Therefore, this study introduces the wound potential-pair continuum (WPPC) model, which is based on the wound structure including a single pair of current collector layers in a finite volume. The definition of the WPPC is explained in the next section.

General geometries of cylindrical cells are featured in Fig. 3(a) and (b). A pair of current collectors coated on both sides by active electrode material is wound with separators, which prevent electrical contact between the opposite electrodes. The cell geometry in Fig. 3(a) has opposite current collector polarity on the innermost and outermost sides, and the same number of wound turns for both collectors. If one current collector had one more wound turn than the other current collector, the cell would have the same polarity on the innermost side and the outermost side, as shown in Fig. 3(b). There are two electrode pairs in both wound geometries in Fig. 3(a) and (b), the inner electrode pair and the outer electrode pair.

During a typical cylindrical cell manufacturing process, a stack of paired current collectors coated with electrodes on both sides and two separators is prepared as sketched in Fig. 3(c). Before winding, a single pair of electrodes is placed between the stacked current collectors, called the inner electrode pair. At this point, the two
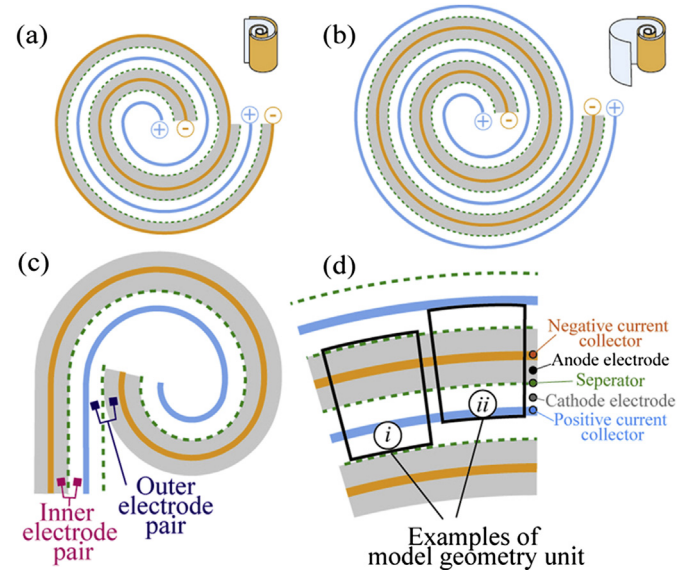
Fig. 3. Examples of an actual wound jelly roll with (a) the opposite polarities, and (b) the same polarity current collectors on the innermost and the outermost layers; description of wound geometry in cylindrical cells − (c) formation of the inner electrode pair and the outer electrode pair in wound geometry, and (d) definition of the model geometry unit.

Cell with continuous tabs

Cell with discrete tabs

Fig. 2. Impacts of tab design on electric current in current collectors: (a) cell with extended-metal-foil-type continuous current tabs, (b) cell with localized discrete tabs.

electrodes coated on the outer sides of the current collectors remain unpaired. These electrodes contact each other during the winding process, forming the second electrode pair, called the outer electrode pair in this study. The wound jelly roll structure of cylindrical cells consists of repeated inner and outer electrode pairs with current collectors. Each electrode pair is operated with distinguished electric potential difference across the current collectors. In modeling wound geometries of cylindrical cells, a model geometry unit is defined as a sandwiched cell composite. Multiple variations of the model geometry unit are possible by inscribing a single pair of current collectors and two electrode pairs, as shown by examples i and ii in Fig. 3(d). Computational grids for the WPPC are built with the model geometry unit, and the WPPC continuum properties are dependent on this unit.

Fig. 4(a) shows the three-dimensional wound cell composite modeled in this study. The chosen model geometry unit is a strata consisting of the following layers: cathode electrode–positive current collector–cathode electrode–separator–anode electrode–negative current collector–anode electrode–separator, in order from the inside of the wound cell to the outside, as shown by example i of Fig. 3(d). The model geometry presented in Fig. 4(b) is the model geometry unit wound in continuous semi-circles with unit thickness l_{cell}. To get continuously connected wound geometry, two groups of concentric semi-circles with two different origins, O_1 and O_2, are attached to each other. The origins of the two groups of concentric semi-circles have a distance of $l_{cell}/2$, and the radii of the two groups are subsequently increased by l_{cell} for continuous attachment. Each region in which a group of concentric semi-circles is laid is defined by the separate coordinate origins $O_1(r_1, \theta_1)$ and $O_2(r_2, \theta_2)$. The advantage of the concentric semi-circular winding model over other spiral geometry models is in its easy orthogonal grid adoption, resulting in better numerical stability with reduced geometrical complication. Once a model geometry unit and computational grid is generated, the cell composite is considered a "continuum", regardless of the specific layer geometry of the individual cell components. The cell domain model then solves the temperature and current collector phase electric potentials, and computes their volumetric source terms as presented in Fig. 4(c).
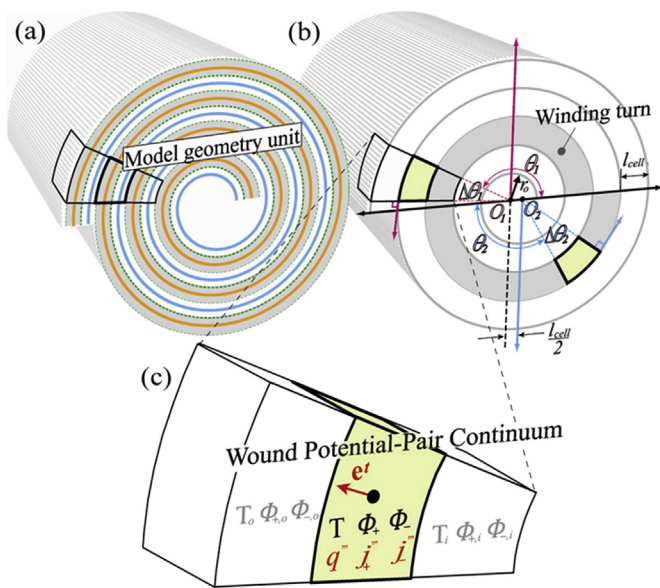
Fig. 4. The WPPC model approach in the present study; (a) define the model geometry unit, (b) construct the wound geometry along continuous concentric semi-circles, and (c) evaluate the solution variables as cell-domain continuum quantities.

2.2. Wound continuum model in cell domain

In the previous study [15], the single potential-pair continuum (SPPC) model was introduced, solving temperature, T, and a single pair of current collector phase electric potentials, Φ_- and Φ_+, in an orthotropic continuum of the cell composite. Detailed strata structure of the composite electrode coating layers, separator films, and current collector foils is not distinguished in an arbitrary finite volume of the cell composite, but treated as a continuum with distinguished in-plane and transverse thermal and electrical transport properties, with the following conditions:

i) In an arbitrary finite volume of the cell composite, transverse direction vector $\mathbf{e}^t$ can be uniquely determined, and

ii) In an arbitrary finite volume of the cell composite, Φ_- and Φ_+ can be uniquely determined.

These conditions are valid for cell systems where layer-to-layer differences in electric potential are negligible, such as aligned stack cells or wound cells with extended foil-type continuous current tabs. The SPPC model, however, is not applicable to wound cells with discrete electrical tabs. Electrical current flowing in the azimuthal direction causes significant variation in electric potential along the current collector phase of the cell composite in the azimuthal direction. To resolve electrical current pathways along the current collectors and electrostatic potential differences across the composite electrode pair boundaries in this cell format, the wound potential-pair continuum (WPPC) model is developed with the following conditions:

i) Model geometry can be defined to include one positive current collector, one negative current collector, and two electrode pair sandwiches.

ii) In a finite volume of the cell composite, transverse direction vector $\mathbf{e}^t$ can be uniquely determined.

iii) In a finite volume of the cell composite, Φ_- and Φ_+ can be uniquely determined.

The unit transverse direction $\mathbf{e}^t$ of the WPPC model is defined as a function of location in the cell composite volume. In this study, for example, it is determined in corresponding coordinate system $O_i(r_i, \theta_i, z_i)$ as

$$\mathbf{e}^t(r_i, \theta_i, z_i) = \widehat{i}_{r_i}, \tag{1}$$

where $\widehat{i}_{r_i}$ is the unit vector of the radial direction in the coordinate system O_i and subscript i is the index of the coordinate system, which can be 1 or 2 in this study. Note that the coordinates $O_i(r_i, \theta_i, z_i)$ are attached to the cell composite continuum object as shown in Fig. 4(b) and point $P_i(r_i, \theta_i, z_i)$ is defined at the center of the finite volume.

In the MSMD model framework, a cell domain submodel, such as the WPPC model, calculates temperature T and current collector phase electric potentials Φ_- and Φ_+, and imposes them onto the electrode domain submodel for computing heat source q''', and electric current sources, j'''_-, j'''_+ [15]. Electrostatic potential fields, Φ_- and Φ_+, in the object-attached coordinate system $O_i(r_i, \theta_i, z_i)$, are computed from charge conservation in the current collectors of the cell components and the passive components outside the cell composite,

$$\left(\frac{\varepsilon_- \sigma_-}{r_-^2} \frac{\partial^2 \Phi_-}{\partial \theta^2} + \varepsilon_- \sigma_- \frac{\partial^2 \Phi_-}{\partial z^2} + j'''_- \right)_i = 0 \tag{2}$$

$$\left(\frac{\varepsilon_+ \sigma_+}{r_+^2}\frac{\partial^2 \Phi_+}{\partial \theta^2} + \varepsilon_+ \sigma_+ \frac{\partial^2 \Phi_+}{\partial z^2} + j_+'''\right)_i = 0 \tag{3}$$

where j_-''', j_+''' denote the volumetric current sources in each current collector phase, and ε_-, ε_+ are the volume fractions of the metal current collectors in the cell composite volume, and σ_-, σ_+ are the electrical conductivity of the current collector components. In addition, r_+ and r_- are the radial locations of each phase current collector in a specific volume and it is defined according to the model geometry unit as:

$$r_+ = r + \frac{l_-}{2} - l_s - l_a, \tag{4}$$

$$r_- = r + \frac{l_+}{2} + l_s + l_c. \tag{5}$$

Equations (2) and (3) imply that the radial conductivity of a cell composite is zero, so that the current doesn't flow in the radial direction across electrode composite layers. At the interfaces between region 1 and region 2, flux continuity condition is applied. Mathematical expressions are:

$$(\nabla \Phi_-)_1 = (\nabla \Phi_-)_2, \tag{6}$$

$$(\nabla \Phi_+)_1 = (\nabla \Phi_+)_2. \tag{7}$$

To obtain volumetric current sources j_-''' and j_+''', electrode plate current density $\overline{\overline{i_x''}}$, which is evaluated in the electrode domain submodel by solving lithium diffusion dynamics and charge transfer at electrode porous media, is converted with relations,

$$j_-''' = -\left(\overline{\overline{i_x''}}a_s\right)_{iep} - \left(\overline{\overline{i_x''}}a_s\right)_{oep,o}, \tag{8}$$

$$j_+''' = \left(\overline{\overline{i_x''}}a_s\right)_{iep} + \left(\overline{\overline{i_x''}}a_s\right)_{oep,i}, \tag{9}$$

where specific electrode plate area a_s in cell composite volume is a continuum property calculated as a cell domain parameter. The subscript iep denotes the inner electrode pair, and the subscripts oep,i and oep,o refer to the outer electrode pairs located at the inner side and outer side of the finite volume, respectively. Schematics in Fig. 5(a) shows the relationships among current source terms and electrochemical processes in two distinguished electrode pairs of the wound cell composite continuum. Electrode plate current densities, $\overline{\overline{i_x''}}$, in Equations (8) and (9) are obtained from the electrode domain submodel using electrical potential Φ_- and Φ_+ as inputs. The subscript x denotes a source term calculated from the

electrode domain in the MSMD model framework [15]. The inner electrode pair $(\overline{\overline{i_x''}})_{iep}$ is calculated with electrical potentials Φ_- and Φ_+ in the designated finite volume through the coupled electrode domain submodel as presented in Fig. 5(b). Meanwhile, to evaluate electrode plate current densities of the outer electrode pair, $(\overline{\overline{i_x''}})_{oep,o}$ and $(\overline{\overline{i_x''}})_{oep,i}$, electric potentials of adjacent finite volumes, $\Phi_{+,o}$ and $\Phi_{-,i}$, are engaged in calculations. The cell output current I_o is the volume integration of the current source over the entire cell composite volume,

$$I_o = \int j_+''' dV = -\int j_-''' dV. \tag{10}$$

Even though the continuum model geometry doesn't resolve individual layers of the cell composite, cell continuum properties of the WPPC, such as effective conductivity, which is a function of the radial locations of the current collectors r_+, r_-, and specific electrode plate area a_s, are determined in relation to the electrode layer geometry dimensions. In this study, the model geometry unit is chosen as shown in Fig. 4(a) and thus, the specific electrode plate area a_s, defined as the midpoint in thickness of the electrode pairs, is calculated as,

$$(a_s)_{iep} = \frac{1}{l_{cell}}\left(1 + \frac{1}{2r}(l_+ - l_- + l_c - l_s - l_a)\right), \tag{11}$$

$$(a_s)_{oep,i} = \frac{1}{l_{cell}}\left(1 - \frac{1}{2r}(l_+ + l_- + l_c + 3l_s + 3l_a)\right), \tag{12}$$

$$(a_s)_{oep,o} = \frac{1}{l_{cell}}\left(1 + \frac{1}{2r}(l_+ + l_- + 3l_c + 3l_s + l_a)\right), \tag{13}$$

where l_{cell} is the thickness of the model geometry unit, l_- and l_+ are the thickness of the negative and positive current collectors, and l_c, l_s and l_a represent the thickness of the cathode electrode, separator, and anode electrode, respectively. Note that specific electrode plate area a_s is a function of location, r. Energy conservation in the object-attached coordinate system $O_i(r_i, \theta_i, z_i)$ yields

$$\left(\frac{\partial(\rho C_p T)}{\partial t} - \frac{1}{r}\frac{\partial}{\partial r}\left(k_{tr}r\frac{\partial T}{\partial r}\right) - \frac{k_{in}}{r^2}\frac{\partial^2 T}{\partial \theta^2} - k_{in}\frac{\partial^2 T}{\partial z^2} - q''' = 0\right)_i, \tag{14}$$

where k_{in} is the in-plane thermal conductivity, k_{tr} is the transverse thermal conductivity of the cell composite, and ρC_p is the volumetric thermal capacity. The volumetric heat source in the cell domain model, q''', includes heat sources evaluated from the electrode domain submodel, as well as joule heat from Ohmic resistance of conductive components in the cell domain.

$$q''' = q_x''' + q_\Omega''' \tag{15}$$

Volumetric heat sources from the electrode domain model, q_x''', are obtained as

$$q_x''' = \left(\overline{\overline{q_x''}}\varepsilon_{ep}\right)_{iep} + \left(\overline{\overline{q_x''}}\varepsilon_{ep}\right)_{oep,i} + \left(\overline{\overline{q_x''}}\varepsilon_{ep}\right)_{oep,o}. \tag{16}$$

Joule heat caused by electronic current in passive components is calculated as

$$q_\Omega''' = q_-''' + q_+''' = \varepsilon_- \sigma_-\left(\left(\frac{1}{r_-}\frac{\partial \Phi_-}{\partial \theta}\right)^2 + \left(\frac{\partial \Phi_-}{\partial z}\right)^2\right)$$
$$+ \varepsilon_+ \sigma_+\left(\left(\frac{1}{r_+}\frac{\partial \Phi_+}{\partial \theta}\right)^2 + \left(\frac{\partial \Phi_+}{\partial z}\right)^2\right). \tag{17}$$
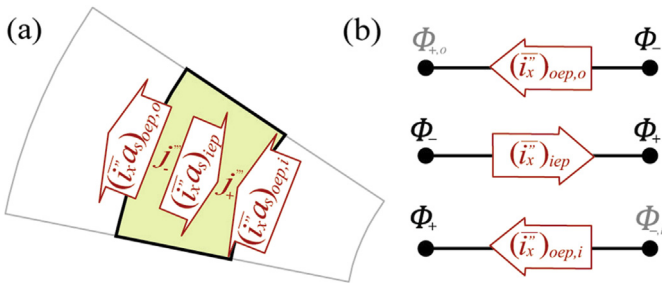

Fig. 5. Relation between (a) electrical current sources from two distinguished electrode pairs, and (b) current collector phase potentials evaluated in cell composite continuum.

The sum of the volume fractions of each component should be unity.

$$(\varepsilon_{ep})_{iep} + (\varepsilon_{ep})_{oep,i} + (\varepsilon_{ep})_{oep,o} + \varepsilon_+ + \varepsilon_- = 1 \quad (18)$$

Temperature fields obtained by solving Equation (12) are given to the electrode domain model as input to evaluate electrode plate current density, $\overline{i''_x}$. However, since the outer electrode pair straddles two different finite volumes by definition of the model geometry unit, volume-averaged temperature of the outer electrode pair in two neighboring finite volumes is used in the electrode domain model. First-order implicit temporal discretization is used for time integration, and the solutions are coupled through Picard iteration.

3. Analysis and results

Using the WPPC cell domain model in the MSMD framework, two case studies are conducted to evaluate the impacts of macroscopic cell design features. The first case is a comparison of cell designs with different numbers of tabs during 80 A (4 C-rate, nominal) constant current discharge. Five different cell designs — cells with continuous-tabs, 20-tabs, 10-tabs, 5-tabs and 2-tabs — are proposed. They are identical in macroscopic cell dimensions and capacity, as well as materials and electrode-level designs. Cell dimension is 130 mm in height, 45 mm in outer diameter, and 8 mm in inner diameter, as shown in Fig. 6(a). The model geometry unit has 39 wound turns, and is about 3.23 m long in unwound length. The capacity is computed as 19.86 Ah, based on the

Fig. 6. Schematics of 20 Ah cylindrical cell design investigated: (a) dimensions and boundary conditions, (b) tab locations in current collectors in wound view (right) and in unwound view (left).

stoichiometric window, and the amount of active material in each cell. The 10 mm-wide electric tabs are distributed evenly along the top and the bottom sides of the unwound electrodes — positive tabs on the top, and negative tabs on the bottom. The second case study investigates the thermal behavior of cells in long-term period use. A simulated geometric voltage pulse cycle is carried out for the 10-tab cell until the system reaches a thermal quasi-steady state. A convective thermal boundary condition is applied on the side of cylindrical cell surfaces with heat transfer coefficient of 25 W m^{-2} K^{-1}, and 25 °C ambient temperature in all cases. We assume that the top and bottom surfaces of all cells are thermally insulated, and the cells are initially at ambient temperature. The input parameters for the sub-domain models in this study are summarized in Table 2, and the input parameters not shown in Table 2 are the same with those presented in Kim et al. [15].

3.1. Comparison of cell responses with different tab numbers during constant discharge

Five cylindrical wound cells, each with a different number of tabs — continuous tabs, 20 tabs, 10 tabs, 5 tabs, and 2 tabs from each current collector foil — are modeled to investigate the impacts of macroscopic electrical pathway design. Fig. 6(b) shows the locations of the tabs in the current collectors in an unwound view (left) and a wound view (right). The tabs are evenly distributed along the top edge of the positive current collectors, and along the bottom edge of the negative current collectors. In this wound geometry, the negative current collectors have larger radii than the positive current collectors and are about 5 cm longer than the positive current collectors; thus, the locations of the tabs are slightly different between the positive and negative current collectors. Simulations of the five cells with different tab numbers are conducted for 80 A (about 4 C-rate) constant current discharge until the cell voltage reaches the cut-off value, 2.5 V. All discharge processes start from 100% state of charge (SOC).

Apparent output voltage curves of the investigated cells are presented for discharge capacity in Fig. 7. As the continuous tab design is believed to be the least resistive for given form factor cells, voltage differences from the continuous-tab cell are regarded as a measure of inefficiency caused by discrete tab design at the simulated C-rate condition. The result shows the lower output voltage for a cell with fewer tabs. The voltage differences from the continuous-tab cell remain relatively constant during discharge — about 7 mV, 20 mV, 50 mV, and 180 mV for a 20-tab cell, 10-tab cell, 5-tab cell, and 2-tab cell, respectively. Increase in cell impedance in cells designed with fewer tabs originates mostly from increased ohmic resistance in the current collectors. Unless the electric path design is unusually poor, this type of overpotential is largely linear to the cell's output current. The model discharge curves shown in Fig. 7 follow the tendency of common observations, quantifying the inefficiency caused by a cell's design. This quantified information is useful for cell design optimization, since cell impedance reduction through increasing the number of electrical tabs increases complexity and manufacturing cost with decreased reliability. Even though cell discharge resistance varies sensitively with the number of tabs, discharge capacities of the cells investigated are similar to 19.2 Ah. The resistive 2-tab cell shows even slightly larger discharged capacity than the others due to the elevated system temperature energizing kinetics and diffusion [21].

Thermal responses of the investigated cells are presented in Fig. 8. The 2-tab cell shows its average volume temperature reaches 35 °C at the end of discharge, while temperature increases in the other cells are less than 20 °C. Excessive energy loss due to inefficient design of the 2-tab cell is converted to heat, raising the cell temperature prominently higher than the other cells. Increasing
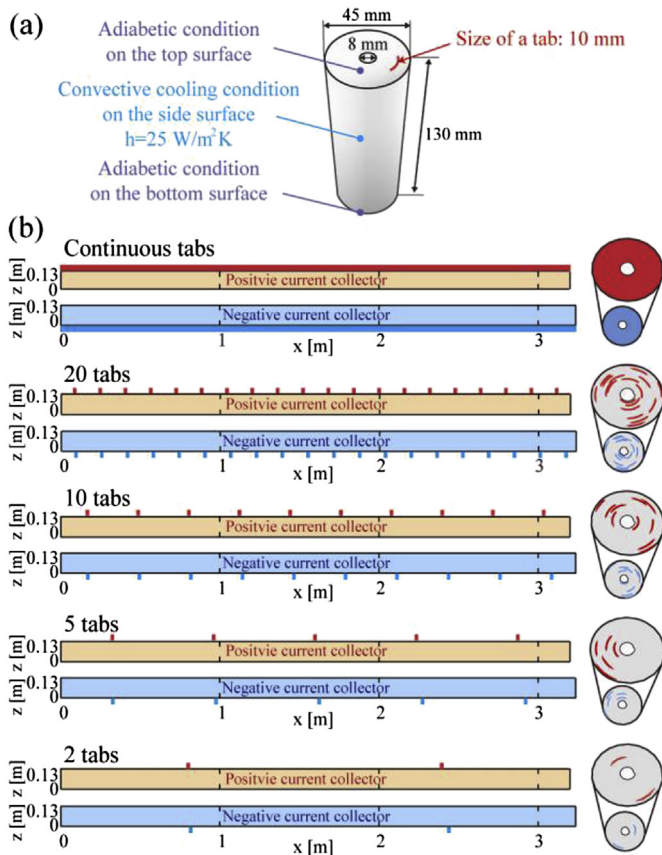
Table 2
Summary of model parameters in submodel choices.

Domain	Parameter		Value/model	
Particle			Li_xC_6	$Li_y(NCA)O_2$
Refs # [17], [18]	Maximum Li capacity, $c_{s,max}$ [mol m^{-3}]		2.87×10^4	4.90×10^4
	Characteristic diffusion length, R_s [m]		$3\varepsilon_s/a_s$	$3\varepsilon_s/a_s$
	Stoichiometry at 0% SOC, $x_{0\%}, y_{0\%}$		(0.0402)	0.98
	Stoichiometry at 100% SOC, $x_{100\%}, y_{100\%}$		0.63	0.41
	Reference exchange current density at 100% SOC, i_o^{ref} [A m^{-2}]		36.0	4.0
	Activation energy, $E_{act}^{i_o}$ [J mol^{-1}]		3.0×10^4	3.0×10^4
	Charge-transfer coefficients, α_a, α_c		0.5, 0.5	0.5, 0.5
Electrode		Negative electrode composite	Separator	Positive electrode composite
Refs # [18], [19]	Thickness, l_a, l_s, l_c [m]	110.0×10^{-6}	25×10^{-6}	80.0×10^{-6}
	Thickness unit stack, l_{asc} [m]		$l_a + l_s + l_c$	
	Volume fraction inert, ε_f	0.07	0.5	0.15
	Volume fraction electrolyte, ε_e	0.45	0.5	0.45
	Volume fraction active material, ε_s	0.48		0.4
	Specific active surface area, $a_{s,x}$ [m^2 m^{-3}]	(2.83×10^6)		(0.735×10^6)
Refs # [20], [19]	Solid electronic conductivity, σ_a, σ_c [S m^{-1}]	100.0		10
	Bruggeman tortuosity exponent, p	1.5	1.5	1.5
	Electrolyte concentration, c_e [mol m^{-3}]		1.2×10^3	
Cell		Negative current collector		Positive current collector
	Thickness, δ_-, δ_+ [m]	15.0×10^{-6}		20.0×10^{-6}
	Specific electrode plate area, $a_{s,\Theta}$ [m^2 m^{-3}]		$(l_{asc} + 0.5\delta_- + 0.5\delta_+)^{-1}$	
	Volume fraction, $\varepsilon_-, \varepsilon_+$	$0.5\delta_-\ a_{s,\Theta}$		$0.5\delta_+\ a_{s,\Theta}$
	Conductivity, σ_-, σ_+ [S m^{-1}]	59.6×10^6		37.8×10^6
	Electrode plate area, $A_{\Theta,p}$ [m^2]		0.8291	
	Volume, cell composite, $V_{\Theta,cc}$ [m^3]		$A_{\Theta,p}/a_{s,\Theta}$	
	Volumetric heat capacity, cell composite, ρc_p, [J K^{-1} m^{-3}]		2.04×10^6	
	Planar thermal conductivity, cell composite, k_p [W m^{-1} K^{-1}]		27	
	Transversal thermal conductivity, cell composite, k_t [W m^{-1} K^{-1}]		0.8	

temperatures at the end of discharge for the simulated cells indicate that the system doesn't reach its thermal equilibrium during discharge. This also implies that heat generation dominates the thermal response of the system during the single discharge event for given heat transfer conditions. Fig. 8(b) presents evolution of cell internal temperature differences in the five different cell designs. The model predicts that the 2-tab cell suffers significant internal temperature imbalance, about 16 °C, indicating heat generation is highly localized in the cell. The highly non-uniform thermal response of the 2-tab cell is clearly shown with the other cell cases in wound and unwound views of the temperature contours in Fig. 9. Contour plots present the temperature field in each cell at 5 min after the start of an 80 A constant current discharge. Hot spots appear at the location of the electrical tabs in all cells investigated except the cell with the continuous-tab design. The repeated pattern of the hot spots along the winding direction is caused by radial heat conduction through the layer structures. Heat generated by energized kinetics and ohmic loss for current

Fig. 7. Apparent output voltage comparison among investigated cells with five different tab numbers for 80 A (4 C) constant current discharge.

convergence preferentially raises temperature near the tabs and spreads through the cell composite. The contours presented in wound cell view clearly show the radial heat dissipation starting from the terminal tabs through the layers, as well as the axial and tangential heat dissipation. Meanwhile, the temperature difference between the cell core and the cell surface is fairly small in this one-time discharge simulation. This is because the internal cell temperature profiles are developed by the heat generation and not by the heat transfer in the short-term heating event. Once surface heat transfer becomes critical while approaching thermal equilibrium, significant temperature variation can develop between the core and the surface of a cell because of the poor radial conductivity. This will be discussed further in the following section. Even though large-capacity cylindrical cells are known to suffer with high temperature at the cell core, the present cases in Fig. 9 for short-term discharge show local peak temperatures near the tabs.

Local heat generation includes multiple heat sources, such as reversible heat from kinetics, ohmic heat for carrying ionic and electric current in electrode matrices and electrolyte, and heat for carrying electrical current through current collectors. Geometric factors and transport limitation affect the amount of heat generated. Joule heat for carrying electrical current is relatively small in total magnitude in well-designed systems. However, this heat is most responsible for spatial non-uniformity of heat source, especially in large systems running on high-rate charge–discharge cycles. If the number of tabs, for example, is reduced by factor of n, the local electrical current convergence near the tab increases by factor n. This quickly increases highly-localized ohmic heat for carrying current in the current collector by factor n^2 (by Ohm's law, $q_\Omega = i^2 R$).

Heat source breakdown, shown in Fig. 10, supports this explanation, showing heat from metal current collector phases in the cell composite separately from the other heat sources. Joule heat in metal current collectors is responsible for a larger portion of total heat generation in the cells, with fewer tabs during discharge, and it
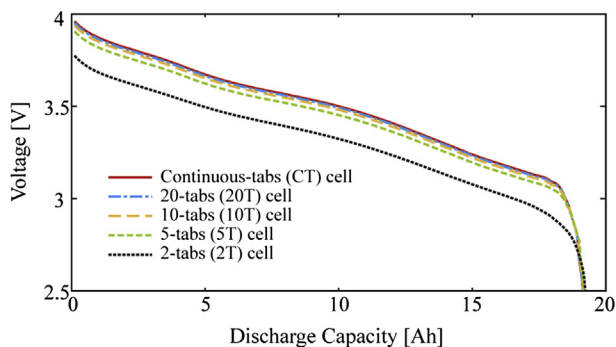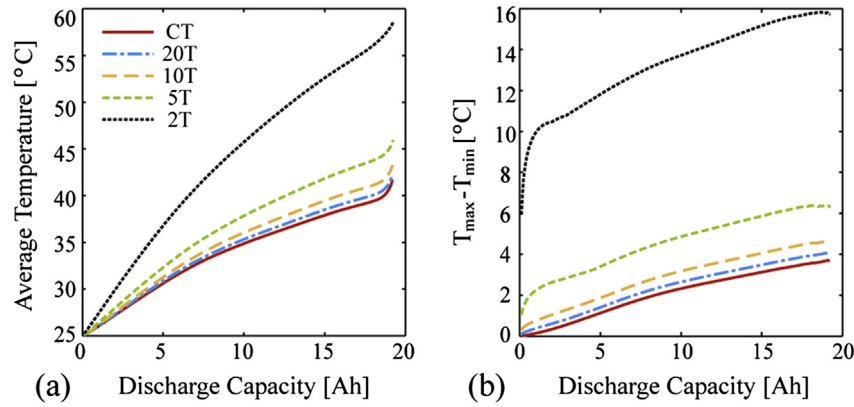
Fig. 8. Comparison of (a) average temperatures and (b) cell internal temperature differences in the five different cell designs during 4 C constant current discharge.
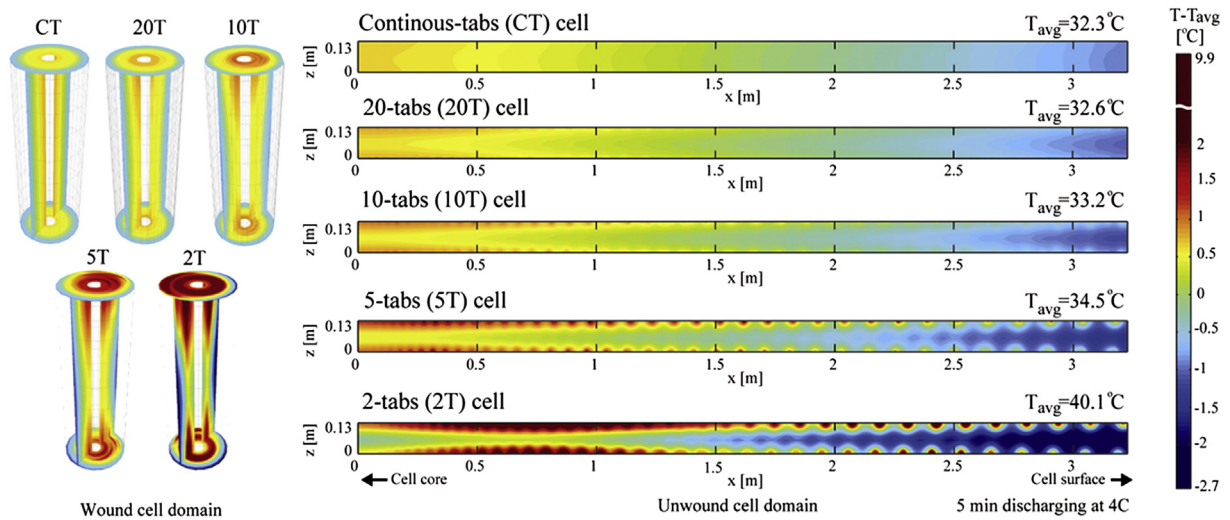

Fig. 9. Temperature contours in wound view (left) and unwound view (right) of the investigated five different cell designs at 5 min after the start of 80 A (4 C) constant current discharge.

leads to an overall increase of heat generation as the number of tabs decreases. All investigated cells are expected to generate a similar amount of heat from the other sources, except the joule heat originating from tab design, but the contribution from these heat sources is shown as decreasing a bit as the tab number decreases. Elevated temperatures experienced by designs with fewer tabs are accompanied by reduced kinetic and transport overpotentials, and consequently, reduced cell electrochemical impedance. Cell
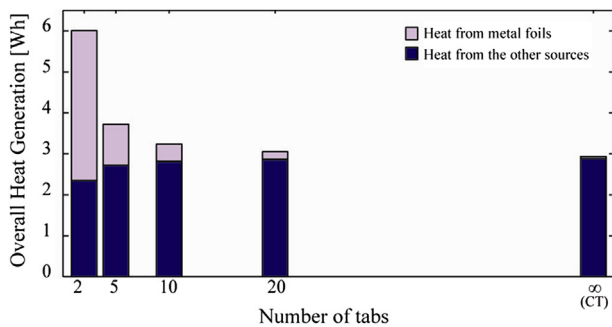
discharge resistances evaluated with the overall heat generation ($R_Q = Q/I^2$) and thermal efficiencies are summarized in Table 3.

Fig. 11 presents the unwound view of the contours of positive and negative current collector phase potential relative to each terminal potential for Φ_+ (a), and Φ_- (b) after 5 min of discharge. Direction and density of electric potential contour lines in Fig. 11 imply clear differences in the pattern of electrical current flow formed in current collectors among the compared designs. The contour lines of the continuous-tab cell are mostly horizontal, while those for the 2-tab design are vertical in both current collectors. This implies that continuous design carries current collector electric current mostly in the axial direction of a wound cell, and that the same current is mostly carried along the winding direction in the 2-tab cell design. Slightly distorted contour lines toward the cell core in the positive current collector, and near the cell surface in the negative current collector of the continuous-tab design, result from the innermost

Fig. 10. Heat source breakdown of the five different cell designs during 80 A (4 C) constant current discharge.

Table 3
Comparison of thermal efficiency and cell discharge resistance.

|	CT	20T	10T	5T	2T
Discharge energy [Wh]	66.71	66.57	66.37	65.97	63.53
Efficiency [%]	95.6	95.4	95.1	94.3	90.5
Total cell discharge resistance [mΩ]	1.91	1.99	2.11	2.45	3.90
Current collector resistance [mΩ]	0.03	0.13	0.28	0.66	2.38
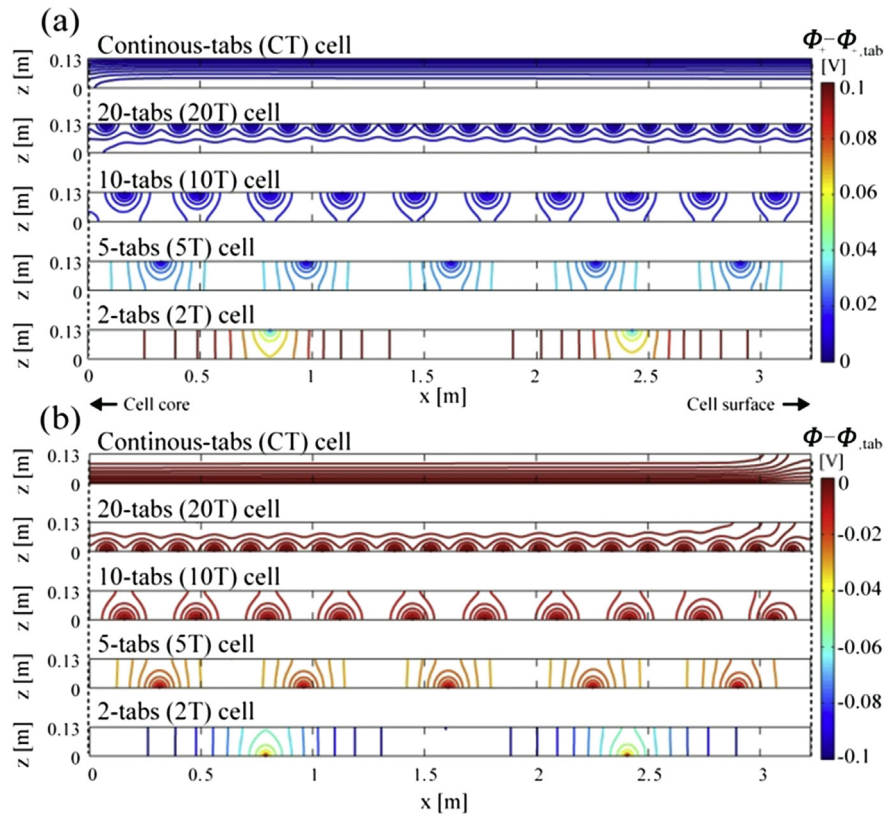
Fig. 11. Contours of current collector phase potentials of cell composite continuum relative to the terminal potential of each five different designs after 5 min discharge at 80 A (4 C) (a) in positive current collectors and (b) in negative current collectors.

and outermost single-side coated current collector portion carrying approximately half of the current as compared with other parts of the cell. Dense contour lines near the tabs originate from rapidly changing electric potential for converging electric current. A typical large-capacity cylindrical cell has very long and continuous electrodes in the winding direction. With limited discrete tabs, the current collectors carry current along long pathways, causing increased cell impedance. More importantly, poor electrical tab design causes exceptional non-uniform kinetics over cell volume, and consequently, non-uniform use of a battery, affecting its life.

Contours of electrode plate current density in Fig. 12 show the distribution of electrochemical reaction over each electrode pair —
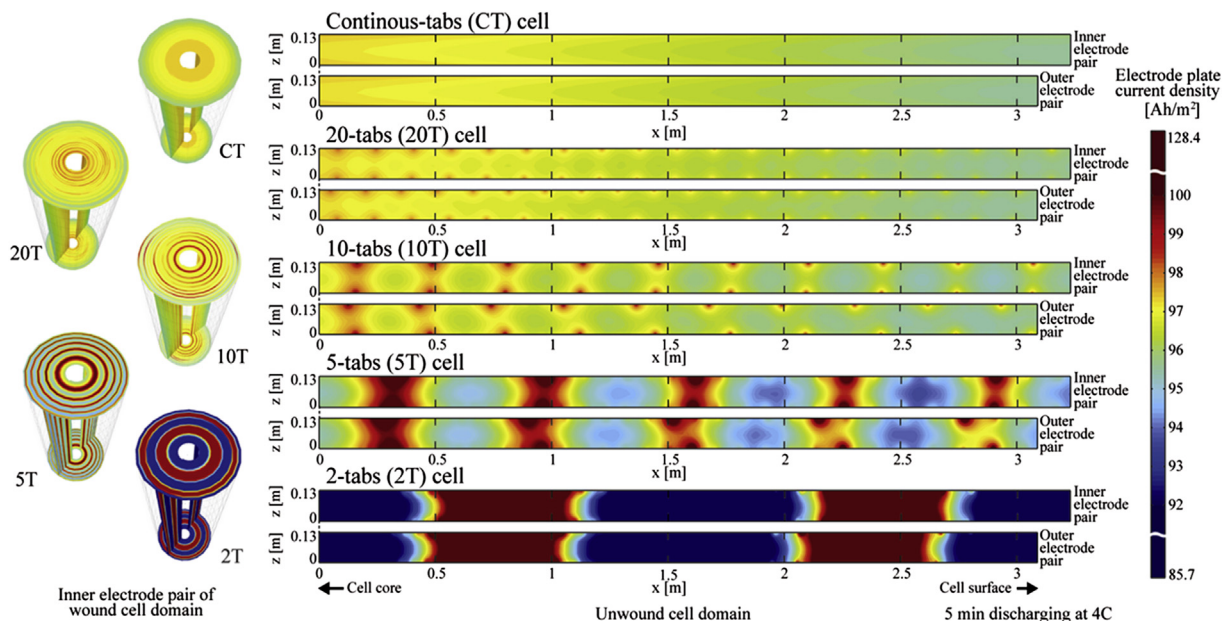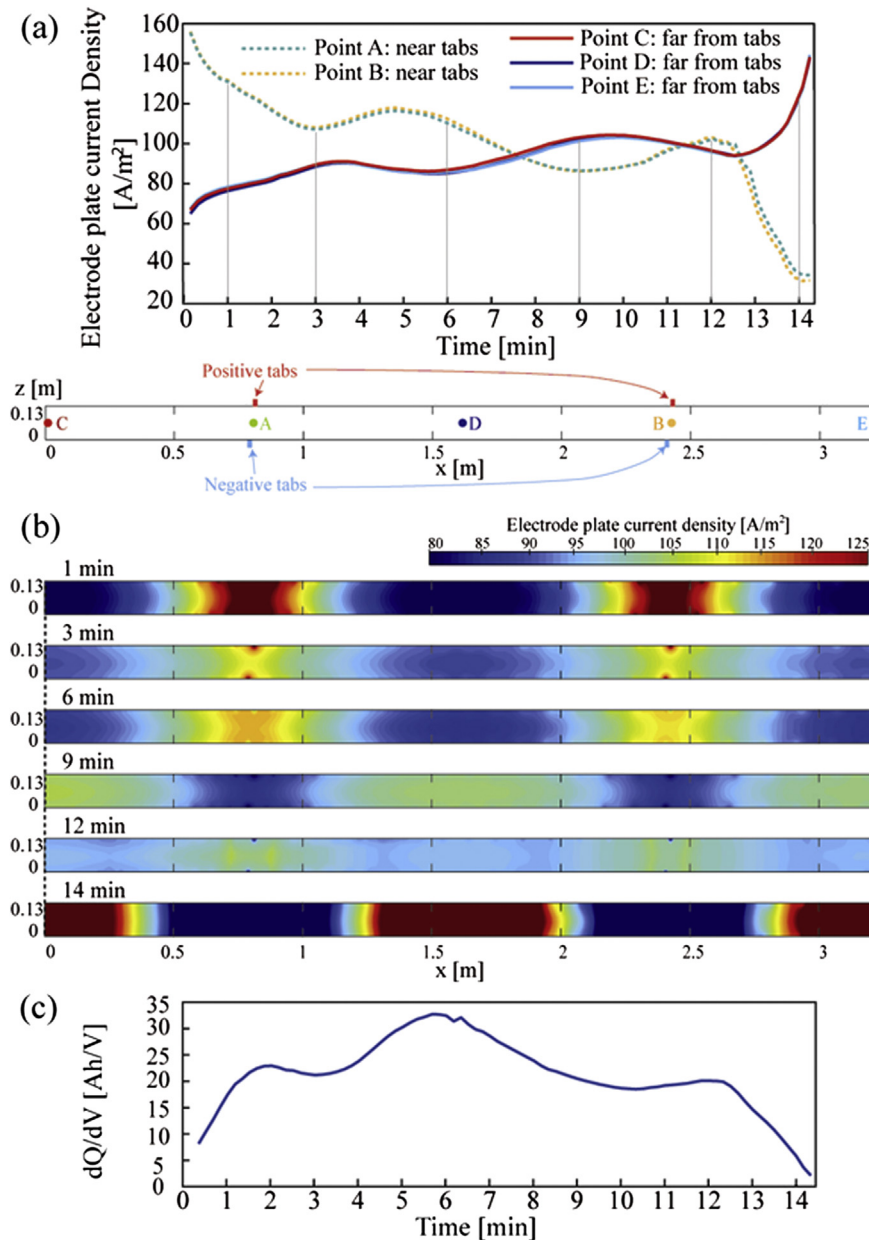

Fig. 12. Contours of electrode plate current density in the five different cell designs after 5 min discharge at 80 A (4 C) in the inner electrode pairs and the outer electrode pairs plotted in unwound view (right), and in wound view for the inner electrode pairs (left).

inner electrode pair and outer electrode pair. In the unwound view of Fig. 12, the outer electrode pair of the investigated cells is seen as being shorter than the inner electrode pair because it has one less winding turn. Note that the locations of the positive tabs attached to the outer electrode pair are shifted toward the cell core by one revolution winding distance because of the unique formation of the outer electrode pair, as illustrated in Fig. 3(c). Discharged capacity of the fully-charged cells is about 19.86 Ah, and the area-averaged electrode plate current density is 96.5 A m^{-2} for an 80 A discharge case. For the instance shown, higher electrode plate current density is found near the tabs. Generally, when a cell runs on pulse cycling or high-rate short-term discharge/charge, near-tab regions of the cell composite are preferentially used. While the electric potential profile is instantly established across the system, relatively slow lithium diffusion dynamics drive the initial non-uniformity of kinetics. Fig. 12 also shows that cells with fewer tabs have larger non-

uniformity of kinetics across the cell volume. While maximum deviation of electrode plate current density in the continuous-tab cell is about 2% of average current density, deviation in the 2-tab cell reaches up to 44%. In cells with many tabs, more energetic kinetics are observed near the cell core than the surface of the cell, and relates directly to the temperature difference.

As mentioned earlier, the spatial distribution of the electrochemical reaction over the electrode pairs keeps changing with time during discharge. Since electrostatic potential distribution along current collectors does not change much during constant current discharge, temporal variation in the electrochemical reaction distribution is mostly derived from the evolution of local thermodynamic status and kinetic and transport limitations. To see the evolution of local electrochemical reaction rates through the discharge process, electrode plate current densities at five evenly-distributed fixed points along the centerline of the inner

Fig. 13. Non-uniform discharge evolution in the 2-tabs cell during 80 A (4 C) discharge: (a) evolution of local electrode plate current density at five evenly distributed locations along unwound electrode (two points near the tabs and three points far from the tabs), (b) contours of electrode plate current density in the inner electrode pair at several instances during discharge, and (c) an inverse curve of discharge voltage slope.

electrode pair of the 2-tab cell are plotted against time in Fig. 13(a). Points A and B are located close to the tabs, while the points C, D, and E are located far from the tabs as shown in Fig. 13(a). Distributions of electrode plate current density in the inner electrode plate at several time points are presented in Fig. 13(b). At the beginning of discharge, electrode plate current density at the points near the tabs is shown as being much larger. While the electric potential profile is quickly established in the current collectors across the cell volume, lithium profiles over a cell develop relatively slowly. Therefore, in the initial stage of discharge, larger kinetic overpotential for more energetic kinetics near the tabs is responsible for non-uniform overpotential distribution across the cell volume. Temperature buildup near the tabs because of localized heating also promotes the imbalance. Spatial imbalance of electrode plate current density decreases during the first 3 min of discharge while concentration profiles are developing in a cell volume. The slope of open-circuit-potential curves against lithium concentration is a major driving force in keeping a system in balance. In a high-slope range, a small difference in concentration can result in a large concentration overpotential difference. While the slope of the open-circuit-potential flattens at about 5 min, the spatial imbalance of the kinetics in the cell increases again as seen in Fig. 13(a). This can be explained by the dQ/dV curve in Fig. 13(c), an inverse of the output voltage slope. The local minimum and subsequent increase of dQ/dV between 3 min and 5 min, indicating decreasing open-circuit-potential slope, also increases the spatial non-uniformity of kinetics in the cell volume. Until about 8 min, deviation in SOC over a cell volume continues to grow because the cell composite near the tabs has continued to discharge current. After that point, the cell's SOC imbalance over its volume starts to decrease. Toward the end of discharge, the near-tab region of the cell composite volume becomes depleted earlier.

3.2. Response of the 10-tab cell during a continuous cycling test

To investigate long-term use cell behavior with development of cell non-uniformity, a simulation of the 10-tab cell was conducted for a voltage-cycle operation. The initial SOC of the 10-tab cell is 0.6, the cell discharges for 11 s at 3.596 V, and then charges for 9 s at 3.825 V periodically over 90 min, as shown in Fig. 14(a). Time-averaged output current is 85.8 A for discharge and 104.6 A for charge for the overall cycling period. Fig. 14(b) shows changes in output current during the operation. At the beginning of cycling, average current is about 71.8 A for discharging and about 85.3 A for charging. SOC of the cell decreases initially because of the imbalance between discharged capacity and charged capacity per cycle, until discharge current is reduced to match the cycled capacity with increased charge current at about15 min of operation. After that time, averaged capacity of the cell remains constant at about 0.584, as presented in Fig. 14(c). However, the amplitude of the output current keeps growing because the increased temperature of the cell enhances the electrochemical process by lowering cell impedance. At around 90 min, the output current of each discharge and charge pulse is stabilized at about 90.0 A and about 110.1 A, respectively.

For the given conditions, it takes about 90 min for the system to reach its thermally-developed state. The thermal responses of the 10-tab cell during the voltage cycle are presented in Fig. 15. When average cell temperature is raised to 52.7 °C, the internal cell temperature difference reaches about 8.3 °C at 90 min. Temperature evolution curves become flat around 90 min in Fig. 15(a), implying the system is thermally developed with an equilibrium average temperature of 52.7 °C. Comparison between heat generation and heat rejection, shown in Fig. 15(b), also confirms that the system reaches its thermal quasi-steady state by 90 min; the 20-
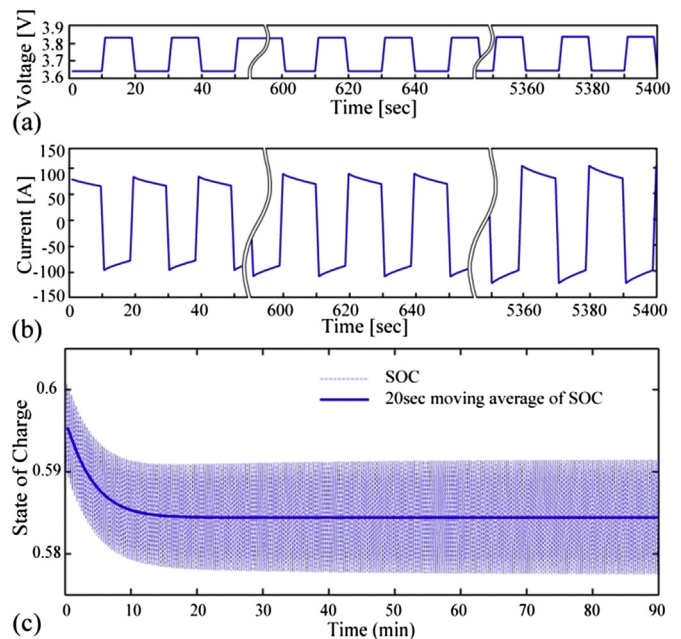

Fig. 14. Voltage cycle operation of the 10-tabs cell for 90 min: (a) apparent voltage profile, (b) output current, and (c) SOC.

s interval average rate of heat generation becomes flat and equal in magnitude to the rate of heat rejection from the system. Efficiency of the cell during the given voltage cycle is 97.0%, and the difference between efficiencies at the beginning and end of the operation is relatively small at 0.03%.

When a cell is cycled for a long period of time, internal cell imbalance of ampere-hour throughput for uneven use of cell materials is accumulated. The preferentially-used portion of a cell would suffer faster and more severe degradation than the rest of the cell composite. Therefore, it is important to understand how the macroscopic electrical and thermal pathway design causes non-
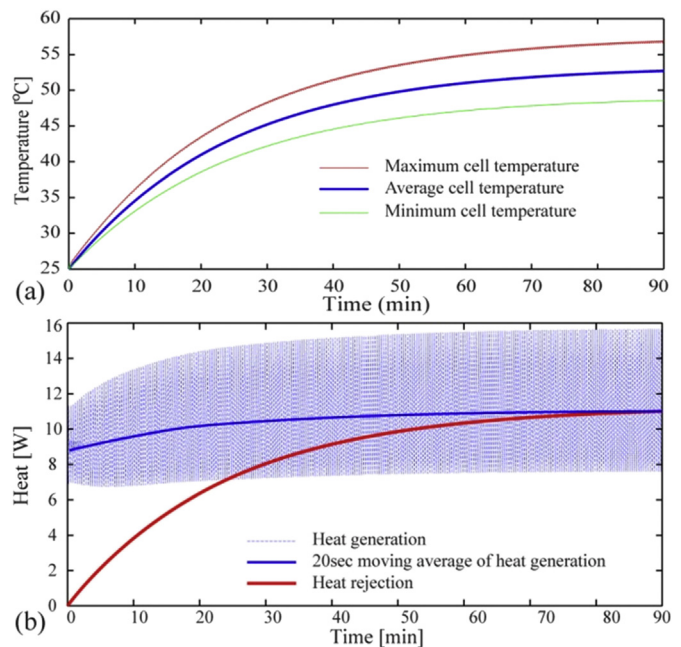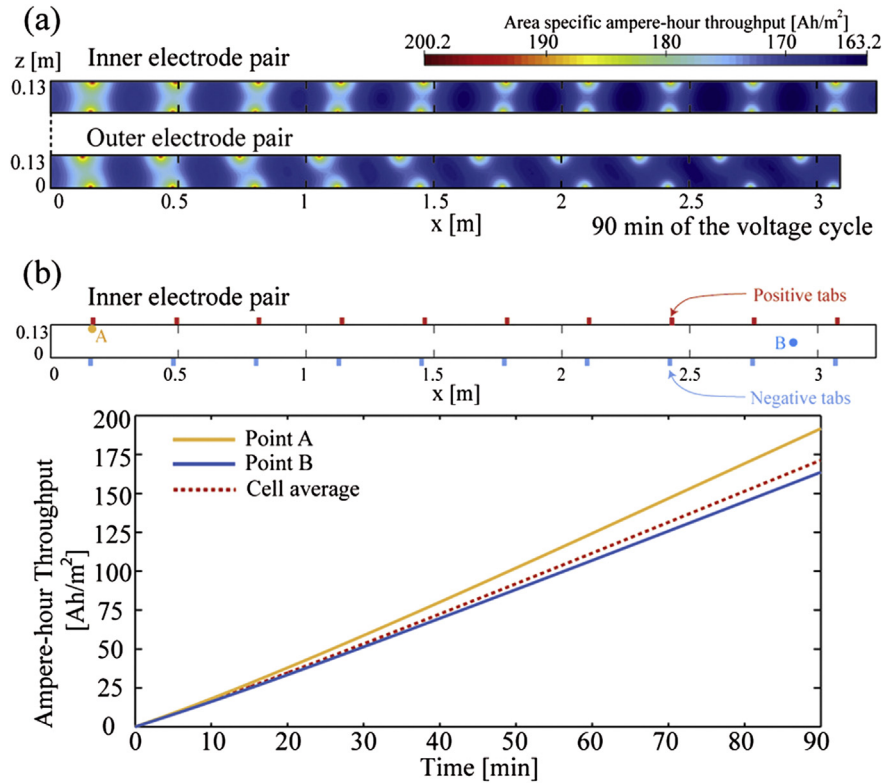

Fig. 15. Thermal responses of the 10-tabs cell during 90 min voltage-cycle operation: (a) evolution of average, maximum and minimum temperature, and (b) comparison between heat generation and heat rejection.

Fig. 16. (a) Distribution of area specific electrode plate ampere-hour throughput in the 10-tabs during 90 min voltage-cycle operation, and (b) comparison between evolution curves of area specific electrode plate ampere-hour throughput at two different locations in a cell.

uniformity over a cell, and to quantify the impact of cell design and operating conditions. Fig. 16(a) shows the distribution of area-specific electrode plate ampere-hour throughput, which is the total coulomb count of discharge and charge current during a 90-min pulse cycle; electrode plate area-averaged throughput is 170.6 Ah m^{-2}. High throughput near the tabs is consistently observed, as already shown by the results from constant discharge cases in the previous section. The 90-min pulse cycle ends up with 17% increased usage near the tabs than the cell average value, a difference proportional to the total cell throughput. Therefore, the accumulated additional throughput at the preferentially-used portion of the cell composite grows continuously over time. The model results also indicate that the cell composite near the wound core is used more than the portion near the cell surface because of the higher temperature inside the cell. Two fixed points (A and B) in the inner electrode pair, where area-specific electrode plate ampere-hour throughput is expected to be close to cell maximum and minimum, respectively, are selected to compare the evolution of the local electrode material usage, as shown in Fig. 16(b). As discussed, the graph confirms that the difference in non-uniform material use in a cell grows proportionally with total battery capacity throughput. The effect of cell degradation is not considered in this study. Anticipated subsequent non-uniform degradation for longer-term use of a cell will critically affect the aging behavior of a cell in close relation with environmental and load conditions. The model introduced in this paper will be applied to investigate complex aging behavior of large-capacity wound cells in following studies.

4. Conclusion

Based on the modularized framework of the MSMD model to resolve various physics occurring at widely ranging length scales in lithium-ion battery systems, the WPPC model was developed as a cell domain submodel and applied to study cylindrically-wound cell behavior. The WPPC model introduces a wound potential-pair continuum (WPPC) to evaluate electrical and thermal transports in wound structures of a cell composite, as well as lithium diffusion dynamics and kinetics across electrode sandwich pairs. Unlike the SPPC model introduced in the previous study [15], which is applicable to wound cells with continuous tabs where layer-to-layer difference of electric potential in current collectors is considered negligible, the WPPC model can be used for simulating wound cells with discrete tabs. The WPPC model allows investigation of the impact of electric tab configuration on wound cell behavior, which is determined by complex interplay among various length-scale physics. In this study, parametric experiments on the number of electrical tabs were conducted by applying the WPPC model. Five different cell designs, with continuous tabs, 20 tabs, 10 tabs, 5 tabs, and 2 tabs, were investigated. The model results indicate that, with a limited number of electrical tabs in a large-capacity cylindrical cell, the current collectors carry current along long pathways, causing increased cell impedance. More importantly, poor electrical tab design causes exceptional non-uniform kinetics over the cell volume, and consequently, non-uniform use of a battery, affecting its life. Continuous pulse-cycling simulation of the 10-tab cell for a voltage cycle revealed how the macroscopic electrical and thermal pathway design causes non-uniformity of kinetics over a cell, and quantified the impact of cell design and operation conditions. The accumulated non-uniformity of material use in a cell tends to increase with battery service life.

Acknowledgments

References

[1] M. Doyle, T. Fuller, J. Newman, J. Electrochem. Soc. 140 (1993) 6.
[2] C.-Y. Wang, V. Srinivasan, J. Power Sources 110 (2002) 364.
[3] K. Kumaresan, G. Sikha, R.E. White, J. Electrochem. Soc. 155 (2008) A164.
[4] Y.I. Cho, G. Halpert, J. Power Sources 18 (1986) 2–3.
[5] T.I. Evans, R.E. White, J. Electrochem. Soc. 136 (1989) 8.
[6] E.E. Kalu, R.E. White, J. Electrochem. Soc. 140 (1993) 23.
[7] S. Al Hallaj, H. Maleki, J.S. Hong, J.R. Selman, J. Power Sources 83 (1999) 1–2.
[8] X. Zhang, Electrochim. Acta 56 (2011) 3.
[9] T.D. Hatchard, D.D. MacNeil, A. Basu, J.R. Dahn, J. Electrochem. Soc. 148 (2001) 7.
[10] Y. Ma, H. Teng, M. Thelliez, SAE Int. J. Engines 3 (2011) 2.
[11] S.-C. Chen, Y.-Y. Wang, C.-C. Wan, J. Electrochem. Soc. 153 (2006) 4.
[12] P.M. Gomadam, R.E. White, J.W. Weidner, J. Electrochem. Soc. 150 (2003) 10.
[13] J.N. Reimers, J. Power Sources 158 (1) (2006) 14.
[14] Y.-S. Chen, K.-H. Chang, C.-C. Hu, T.-T. Cheng, Electrochim. Acta 55 (2010) 22.
[15] G.-H. Kim, K. Smith, K.-J. Lee, S. Santhanagopalan, A. Pesaran, J. Electrochem. Soc. 58 (2011) 8.
[16] K.A. Smith, C.D. Rahn, C.-Y. Wang, Energy Convers. Manage. 48 (2007) 9.
[17] M. Doyle, Y. Fuentes, J. Electrochem. Soc. 150 (2003) A706.
[18] D.W. Dees, E. Gunen, D.P. Abraham, A.N. Jansen, J. Prakash, J. Electrochem. Soc. 155 (2008) A603.
[19] P. Albertus, J. Christensen, J. Newman, J. Electrochem. Soc. 156 (2009) A606.
[20] V. Srinivasan, J. Newman, J. Electrochem. Soc. 151 (2004) A1530.
[21] W.B. Gu, C.Y. Wang, J. Electrochem. Soc. 147 (2000) 8.